



# Adaptive Multi-Command TAEM Guidance Using a Cascade Predictor-Corrector Scheme

Se-Hwan An<sup>1</sup>, Cheol-Goo Jung<sup>1</sup>, Chang-Hun Lee<sup>1</sup>, Hyoung-Sik Choi<sup>2</sup>, Yeon-Deuk Jeong<sup>2</sup>

#### Abstract

This paper presents a Cascade Predictor-Corrector Scheme (CPCS) for the Terminal Area Energy Management guidance of a reusable space vehicle. While numerous guidance algorithms have been developed for the TAEM phase, many suffer from high computational loads or decoupled control strategies that limit real-time performance and optimality. The proposed CPCS addresses these limitations by integrating a cascaded correction logic with a robust in-flight trajectory prediction and refinement process. The guidance architecture sequentially adjusts the reference dynamic pressure profile, Heading Alignment Cone radius, and speedbrake deflection based on a sensitivity analysis that establishes a clear hierarchy of control authority. This cascade structure effectively manages vehicle energy and ground track to satisfy terminal constraints under dynamic flight conditions. The performance of the CPCS is evaluated through nominal and Monte Carlo simulations. The results demonstrate that the algorithm achieves a 99.2% success rate and provides significantly higher accuracy in terminal position and energy control compared to the legacy Space Shuttle guidance algorithm, confirming its robustness and effectiveness.

**Keywords:** Reusable space vehicle, Terminal area energy management, Predictor-Corrector, Guidance

### **Nomenclature**

Latin
OTV – Orbit Test Vehicle

OTV - OTDICTESC VEHICLE

RSV – Reusable Space vehicles

TAEM – Terminal Area Energy Management

A/L – Approach and Landing HAC – Heading Alignment Cone EDC – Energy Dissipation Circle

CPCS - Cascade Predictor-Corrector Scheme

G - Gain

C - Aerodynamics Coefficient

Greek

 $\theta$  – Longitude  $\phi$  – Latitude

 $\gamma$  - Flight-path angle  $\psi$  - Heading angle

 $\Omega$  – Earth's rotational angular velocity  $\mu$  – Earth's gravitational parameters

 $\alpha$  – Angle-of-Attack  $\sigma$  – Bank angle

 $\delta$  – Speed brake angle

Superscripts

p - Proportional

i – Integral

d - Differential

k – Step

new – New Value

nom - Nominal Value

Subscripts

ref – Reference

pred – Prediction

sb - Speed brake

X – X-axis

Y – Y-axis

Z - Z-axis

AT - Acquisition Turn

TAN - Tangency point

HAC - HAC Turn

PF - Pre-final

ALI - Approach and Landing Interface

0 – Initial

<sup>&</sup>lt;sup>1</sup>Korea Advanced Institute of Science and Technology, Daejeon, Republic of Korea

<sup>&</sup>lt;sup>2</sup>Korea Aerospace Research Institute, Daejeon, Republic of Korea

### 1. Introduction

The Boeing X-37B unmanned reusable spaceplane currently supports U.S. Department of Defense missions [1]. Most recently, on its eighth orbital mission (OTV-8), the vehicle was launched aboard SpaceX's reusable Falcon 9 launch vehicle to conduct two primary technology tests: high-bandwidth inter-satellite laser communications and enhanced non-GPS navigation utilizing a high-performance quantum inertial sensor. These experiments underscore the versatility of reusable spaceplanes across a wide range of applications. Reusable launch vehicles have become the most frequently flown platforms, and their low per-launch cost continues to drive extensive development in both government and commercial sectors.

The genesis of reusable space vehicles (RSV) traces to NASA's Space Shuttle program, whose reentry guidance algorithms continue to serve as the foundation for contemporary research. The Shuttle's entry guidance architecture comprises three distinct phases—Entry Interface, Terminal Area Energy Management (TAEM), and Approach and Landing (A/L)—each fulfilling a specific mission objective. The TAEM phase bridges reentry and A/L by managing the orbiter's energy to optimize landing conditions and aligning its heading with the runway centerline [2]. The Space Shuttle's TAEM guidance was based on an offline-designed ground track and a reference-altitude tracking scheme to provide wind-robust performance, enabling successful mission completion [3]. However, because the trajectory was generated offline, it could not readily accommodate real-time environmental changes, prompting numerous follow-on studies.

Various TAEM guidance techniques and ground-track generation methods have been proposed.

### These include:

- adjusting angle of attack and flight-path angle to track a pre-planned dynamic pressure profile while generating the ground track onboard using the segmented-snake concept [4];
- employing the Space Shuttle's ground-track method and tracking a reference altitude profile composed of two quadratic polynomials [5];
- tracking dynamic pressure while regenerating the trajectory via optimization under failure conditions [6];
- applying predictor-corrector schemes to update the trajectory in flight [7–10]; and
- analytically regenerating the ground track using the equivalent wings-level range [11].

Many studies adopt the Space Shuttle ground-track generation method described in Ref. [3]. Other approaches include augmenting the heading alignment cone/circle (HAC) with an energy dissipation circle (EDC) to manage energy using two circles [8], extending range through a straight-flight segment [12], defining a geometric ground track with two straight lines and three circles [13], and aligning to the runway using a large-circle and small-circle combination [14].

While numerous guidance schemes have been proposed for the TAEM phase, many rely on computationally intensive algorithms or employ decoupled control strategies, which can limit real-time performance and hinder optimal trajectory generation under dynamic flight conditions. Furthermore, the development of a comprehensive framework that systematically integrates ground-track refinement, energy management, and all available control commands to achieve a robust and efficient guidance solution remains an active area of research. This paper presents a cascade predictor—corrector guidance scheme (CPCS) for the TAEM phase. The approach decouples longitudinal and lateral trajectory commands during generation but integrates them during correction. By sequentially adjusting parameters through conditional refinement, the scheme captures coupling effects across domains, producing a unified three-dimensional trajectory that remains feasible under dynamic flight conditions.

The key contributions of this work are:

• An optimization-based analysis that identifies near-optimal ground-track trajectories among algorithms previously proposed in the literature.

- A cascade-style refinement logic in which ground-track alignment, reference dynamic-pressure
  profiles, and speed-brake target points are sequentially adjusted to generate suitable TAEM
  guidance commands under dynamic flight conditions.
- An expansion of the degrees of freedom in trajectory design by incorporating angle-of-attack, bank-angle, and speed-brake commands into the guidance process.

The remainder of this paper is organized as follows. Section 2 describes the vehicle model and equations of motion. Section 3 details the generation of longitudinal and lateral guidance commands. Section 4 presents the structure and implementation of the proposed CPCS. Section 5 provides simulation-based evaluations, and Section 6 offers concluding remarks.

## 2. Preliminary

### 2.1. Equations of motion

The three-degrees-of-freedom (3DOF) point-mass equations of motion for a re-entry vehicle over a rotating spherical Earth are

$$\dot{r} = V \sin \gamma \tag{1}$$

$$\dot{\theta} = \frac{V\cos\gamma\sin\psi}{r\cos\phi} \tag{2}$$

$$\dot{\phi} = \frac{V\cos\gamma\cos\psi}{r} \tag{3}$$

$$\dot{V} = -\frac{D}{m} - \frac{\mu \sin \gamma}{r^2} + \Omega^2 r \cos \phi \left( \sin \gamma \cos \phi - \cos \gamma \sin \phi \cos \psi \right) \tag{4}$$

$$\dot{\gamma} = \frac{1}{V} \left[ \frac{L \cos \sigma}{m} + \left( V^2 - \frac{\mu}{r} \right) \left( \frac{\cos \gamma}{r} \right) + 2\Omega V \cos \phi \sin \psi + \Omega^2 r \cos \phi \left( \cos \gamma \cos \phi + \sin \gamma \cos \psi \sin \phi \right) \right] \tag{5}$$

$$\dot{\psi} = \frac{1}{V} \left[ \frac{L \sin \sigma}{m \cos \gamma} + \frac{V^2 \cos \gamma \sin \psi \tan \phi}{r} - 2\Omega V \left( \tan \gamma \cos \psi \cos \phi - \sin \phi \right) + \frac{\Omega^2 r}{\cos \gamma} \sin \psi \sin \phi \cos \phi \right]$$
 (6)

where r is the distance from the Earth's center to the re-entry vehicle,  $\theta$  and  $\phi$  denote the longitude and latitude, respectively. V is the Earth-relative velocity, while  $\gamma$  and  $\psi$  are the Earth-relative flight path angle and heading angle, respectively. The heading angle is defined as positive in the clockwise from the north.  $\Omega$  represents the Earth's rotational angular velocity,  $\mu$  is the Earth's gravitational parameter, and m denotes the mass. L and D are the lift and drag forces, respectively, and are given by:

$$L = \frac{1}{2}\rho V^2 S_{ref} C_L (M, \alpha, \delta_{sb})$$
 (7)

$$D = \frac{1}{2}\rho V^2 S_{ref} C_D \left( M, \alpha, \delta_{sb} \right)$$
 (8)

where  $\rho$  is the atmospheric density and  $S_{ref}$  is the reference area of the re-entry vehicle.  $C_L$  and  $C_D$  are the aerodynamic coefficients. M and  $\alpha$  are Mach number and angle of attack, respectively.

### 2.2. Vehicle model

The model employed in this study is based on the X-37B configuration using publicly available data, with the aerodynamic model generated using Missile DATCOM. While aerodynamic coefficients can be expressed as functions of Mach number, angle of attack, and sideslip angle, this study employs a simplified approach where the sideslip angle is held constant at zero degrees, and the speed brake effects are assumed to vary linearly. The lift and drag coefficients are determined by combining lookup tables for Mach number and angle of attack with linear approximations based on speed brake deflection angle.

$$C_X(M,\alpha,\delta_{sb}) = C_{X,0}(M,\alpha) + \Delta C_{X,\delta_{sb}}(M,\alpha)\delta_{sb}$$
(9)

$$C_Z(M, \alpha, \delta_{sb}) = C_{Z,0}(M, \alpha) + \Delta C_{Z,\delta_{sb}}(M, \alpha)\delta_{sb}$$
(10)

$$C_L(M, \alpha, \delta_{sb}) = C_X(M, \alpha, \delta_{sb}) \sin \alpha - C_z(M, \alpha, \delta_{sb}) \cos \alpha$$
(11)

$$C_D(M, \alpha, \delta_{sb}) = -C_X(M, \alpha, \delta_{sb}) \cos \alpha - C_z(M, \alpha, \delta_{sb}) \sin \alpha$$
(12)

During the TAEM phase, all RCS propellant is depleted, and thus control is achieved exclusively through aerodynamic surfaces. Therefore, a fixed mass of  $3,400\,\mathrm{kg}$  is used, with reference area of  $4.4092\,\mathrm{m}^2$ . The destination is Jeju International Airport in South Korea, located at  $33.49985^{\circ}N$  latitude,  $126.46833^{\circ}E$  longitude. The runway azimuth is  $58.2279^{\circ}$ , and altitude is  $36\,\mathrm{m}$  above sea level. The initial conditions correspond to the terminal values of the Entry phase, while the final conditions correspond to the initial values of the Approach and Landing phase, as presented in Table 1. While heating rate constraints are

Table 1. Initial and final conditions of nominal TAEM

Conditions	r, km	$\theta$ , deg	$\phi$ , deg	V, m/s	$\gamma$ , deg	$\psi$ , deg
Initial	6396.5772	126.5720	32.9737	756.7127	-7.4691	-14.6972
Final	6374.0680	126.3616	33.4445	170.2129	-18.1621	-303.0363

eliminated during this flight segment, dynamic pressure and load factor limitations remain to prevent structural damage. Given that this model represents an unmanned vehicle, the constraints are established as  $q_{\rm max}=19,000\,{\rm Pa}$ ,  $q_{\rm min}=8,000\,{\rm Pa}$  and  $n_{\rm max}=4.0\,{\rm g}$ . In addition, both the bank angle and the speed brake deflection were limited to a maximum of  $80^{\circ}$ .

## 3. Longitudinal Guidance

### 3.1. Reference Dynamic Pressure Profile

Dynamic pressure is a function of air density and velocity. Since air density is dependent on altitude, dynamic pressure effectively determines the vehicle's altitude and velocity. Consequently, by tracking a reference dynamic pressure profile, it is possible to satisfy the desired altitude and velocity, which in turn determines the total flight distance. Because dynamic pressure is directly proportional to the aerodynamic load, a suitable reference dynamic pressure profile must be designed to be within the allowable maximum dynamic pressure for structural safety and the minimum dynamic pressure required for maintaining controllability.

Most studies, divide the profile into three segments. The profile typically consists of a third-order polynomial, a constant dynamic pressure segment, and a final third-order polynomial. To achieve this, the reference dynamic pressure polynomial is given by:

$$\bar{q}_{\mathsf{ref}} = \frac{c_1}{3} \left( h - c_2 \right)^3 + c_3 h + c_4$$
 (13)

The polynomial coefficients are derived from continuity conditions, where the derivatives are equal at each transition point to ensure a smooth and continuous profile.

$$c_1 = -\frac{6\left(\bar{q}_i - \bar{q}_{i+1}\right)}{\left(h_i - h_{i+1}\right)^3} \tag{14}$$

$$c_2 = \frac{h_i + h_{i+1}}{2} \tag{15}$$

$$c_3 = -\frac{c_1 \left(h_i - h_{i+1}\right)^2}{4} \tag{16}$$

$$c_4 = \bar{q}_i - \frac{1}{3}c_1 \left(\frac{h_i - h_{i+1}}{2}\right)^3 - c_3 h_i \tag{17}$$

Here, the subscript i denotes the flight phase transition point, where i = 1 or i = 3.

## 3.2. Baseline Longitudinal Guidance Law

Dynamic pressure is expressed as  $\bar{q} = \frac{1}{2}\rho V^2$  and its time derivative is

$$\dot{\bar{q}} = \frac{1}{2}\dot{\rho}V^2 + \rho V\dot{V} \tag{18}$$

Substituting the derivative of the exponential atmospheric density model and Eq. 4 into Eq. 18, while neglecting the effects of Earth's rotation, yields:

$$\dot{\bar{q}} = -\frac{2\bar{q}D}{mV} + \left(-\frac{\bar{q}V}{h_s} - \frac{2\bar{q}g}{V}\right)\sin\gamma = -f_1 + g_1\sin\gamma \tag{19}$$

where the scale height,  $h_s$ , is 7254.24 m. Subsequently, applying feedback linearization with second-order error dynamics for dynamic pressure, the reference flight-path angle is obtained. The second-order error dynamics are adopted because the longitudinal guidance law, as illustrated in Fig. 1, sequentially generates the angle-of-attack command. This sequential process introduces a delay, and the inclusion of an integrator in the second-order error dynamics compensates for the resulting steady-state error.

$$\dot{\bar{q}} = -2\zeta_{\bar{q}}\omega_{\bar{q}} \left(\bar{q} - \bar{q}_{\text{ref}}\right) - \omega_{\bar{q}}^2 \int (\bar{q} - \bar{q}_{\text{ref}})dt$$
(20)

$$\gamma_{\text{ref}} = \sin^{-1} \frac{1}{g_1} \left( 2\zeta_{\bar{q}} \omega_{\bar{q}} \left( \bar{q}_{\text{ref}} - \bar{q} \right) + \omega_{\bar{q}}^2 \int \left( \bar{q}_{\text{ref}} - \bar{q} \right) dt + f_1 \right) \tag{21}$$

Next, the reference flight-path angle is processed using a first-order error equation, from which Eq. 5, under the assumption that the Earth's rotation is neglected, yields the corresponding lift command.

$$\dot{\gamma} = -\frac{g}{V}\cos\gamma + \frac{L\cos\sigma}{mV} = -f_2 + g_2L = \frac{1}{\tau_\gamma}\left(\gamma_{\mathsf{ref}} - \gamma\right) \tag{22}$$

$$L_{\rm cmd} = \frac{1}{\tau_{\gamma}g_2} \left( \gamma_{\rm ref} - \gamma \right) + \frac{f_2}{g_2} \tag{23} \label{eq:Lcmd}$$

The angle-of-attack command that satisfies this lift requirement is then computed via the secant method.

$$\alpha_{\rm cmd} = f(L_{\rm cmd}, \delta_{sh}, Mach) \tag{24}$$

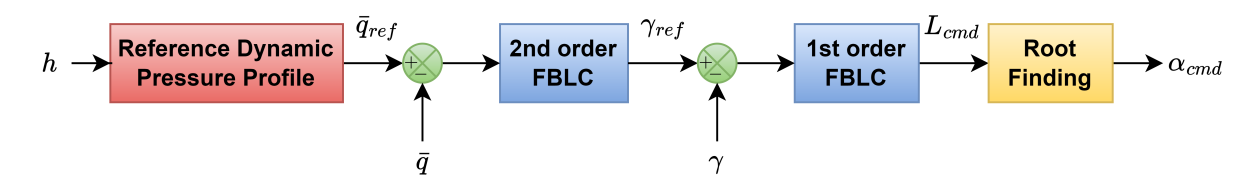


Fig 1. Angle-of-Attack Command Using Feedback Linearization

### 3.3. Speed Brake Guidance Law

In Section 3.2, the drag used to compute the angle-of-attack command is calculated from

$$D = D_0 + D_{\delta^{\mathsf{nom}}} \tag{25}$$

where  $D_0$  is the drag excluding the effect of the speed brake, and  $D_{\delta^{nom}}$  is the drag generated by the nominal speed-brake angle command. Since  $\bar{q}$  is formulated using a second-order error equation, this nominal command alone is sufficient to track the reference dynamic-pressure profile. However, to improve tracking accuracy, the dynamic-pressure error is compensated through an available speed-brake guidance command. This compensation is implemented via a PI controller and becomes active after the HAC turn phase.

$$\delta_{sb} = \delta_{sb}^{\mathsf{nom}} + K_{sb}^{\mathsf{p}} \left( \bar{q}_{\mathsf{ref}} - \bar{q} \right) + K_{sb}^{\mathsf{i}} \int \left( \bar{q}_{\mathsf{ref}} - \bar{q} \right) dt \tag{26}$$

If the vehicle cannot reach the runway even while flying at the minimum reference dynamic pressure,  $\delta_{sb}^{\rm nom}$  is decreased to increase the flight distance. Conversely, if the vehicle overshoots the runway even while flying at the maximum reference dynamic pressure,  $\delta_{sb}^{\rm nom}$  is increased to decrease the flight distance.

### 4. Lateral Guidance

## 4.1. Optimal Ground Track

As previously mentioned, various techniques have been proposed for generating the ground track during the TAEM phase. This study employs an optimization-based approach to find a near-optimal ground track by formulating an objective function that minimizes the reference dynamic pressure profile tracking error, angle-of-attack rate, and bank angle rate.

$$\min_{u} J = \int_{t_0}^{t_f} w_{\dot{\sigma}} \dot{\sigma}^2 + w_{\dot{\alpha}} \dot{\alpha}^2 + w_{\bar{q}} \left( \bar{q} - \bar{q}_{\mathsf{ref}} \right)^2 dt \tag{27}$$

The optimization is performed subject to the initial and final conditions specified in Table 1 and the dynamic pressure and load factor constraints discussed in Section 2.2. The equations of motions Eq. 1 - Eq. 6 are normalized using Earth's radius  $R_E$  for distance,  $\sqrt{g_0R_E}$  for velocity, and  $\sqrt{R_E/g_0}$  for time, where  $R_E=6,370,987.308\,\mathrm{m}$  and  $g_0=9.81\,\mathrm{m/s^2}$ .

The optimal ground track obtained by using Eq. 27 as the objective function is shown in Fig. 2a. In the terminal phase, where the velocity is low and the air density is high, the trajectory shows that greater control authority is used to align the RSV's heading with the runway. The gradually decreasing turn radius is also similar to the shape of the Space Shuttle ground track. As shown in Fig. 2b, the angle-of-attack command that minimizes the error with respect to the reference dynamic pressure maintains a low value throughout the entire flight, resulting in cruise at a high lift-to-drag ratio. Fig. 2c shows that, in order to minimize changes in bank angle, abrupt variations are eliminated, producing a smooth profile that reaches the maximum bank angle.

The optimization aimed to identify an efficient ground track. Comparison with previously proposed ground-track generation algorithms indicated that the Space Shuttle ground track most closely resembled the optimal solution. Therefore, the ground-track generation algorithm in this study was constructed based on the methods presented in Refs. [3, 11].

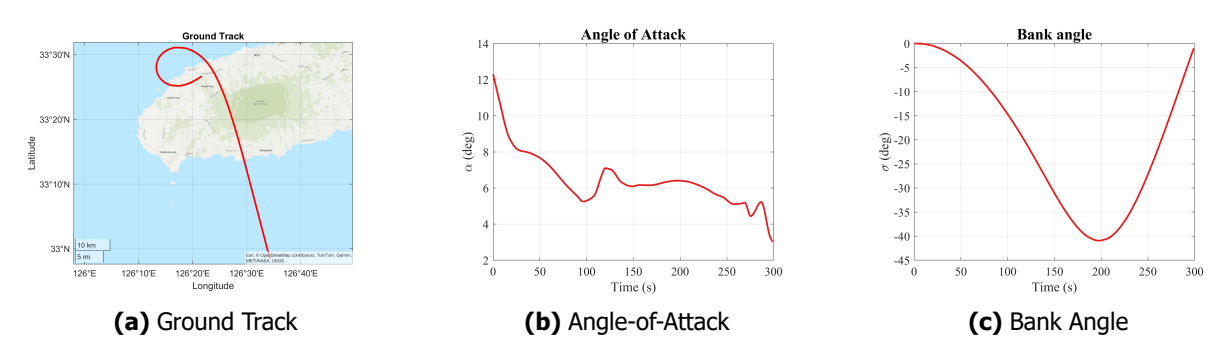


Fig 2. Ground Track Optimization Results

## 4.2. Ground Track Generating Algorithm

The trajectory referenced in the literature can be represented as shown in Fig. 3 Assuming an arbitrary bank-angle command generates a circular trajectory, the trajectory during the acquisition phase is

calculated.

$$R_{AT} = \frac{V_0^2 \cos \gamma_0}{g \tan \phi_{AT}} \tag{28}$$

$$s_1 = R_{AT} |\Delta \psi_{AT}| \tag{29}$$

The vehicle then approaches the HAC along a straight path, which is computed from geometric relations.

$$a = R_{AT}(1 - \cos \Delta \psi_{AT}) \tag{30}$$

$$b = R_{TAN} - R_{AT} |\sin \Delta \psi_{AT}| \tag{31}$$

$$s_2 = \sqrt{a^2 + b^2} {32}$$

The HAC is planned with a spiral shape of decreasing radius, using a fixed  $R_2$  value.

$$R_{HAC} = R_F + R_2 \Delta \psi_{HAC}^2 \tag{33}$$

$$s_3 = R_F \Delta \psi_{HAC} + \frac{1}{3} R_2 \Delta \psi_{HAC}^3$$
 (34)

The pre-final phase consists of a straight path toward the ALI point to align with the runway.

$$s_4 = x_{ALI} - x_{HAC} \tag{35}$$

The total ground distance is predicted by summing the lengths obtained from all these phases.

$$s_{\text{total}} = s_1 + s_2 + s_3 + s_4 \tag{36}$$

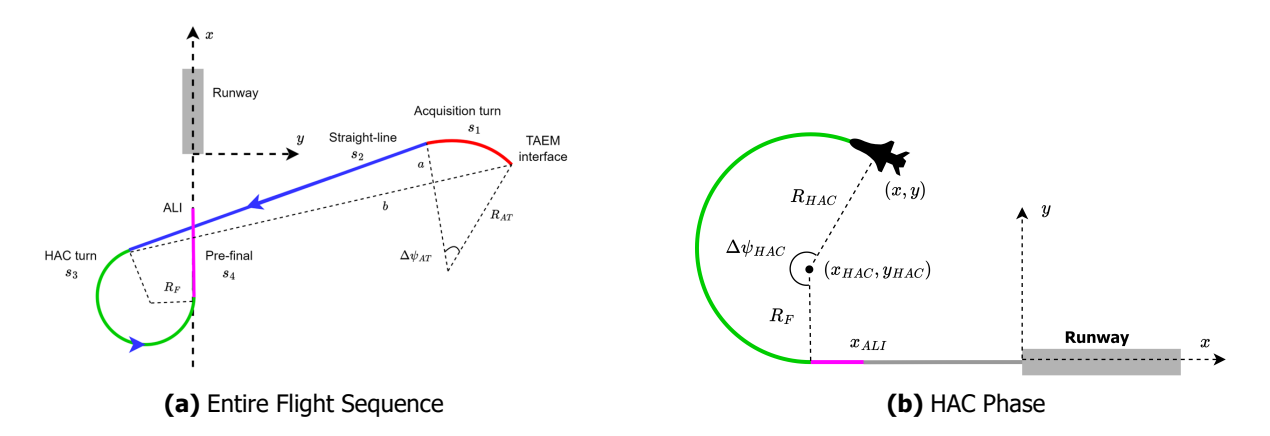


Fig 3. Ground Track Geometry

### 4.3. Lateral Guidance Law

In the acquisition phase, a  $40^\circ$  bank command aligns the vehicle rapidly with the HAC tangency point. Once the heading error falls below  $2^\circ$ , the bank command is computed as the product of the error and a proportional gain.

$$\phi_{AT} = G_{AT} |\Delta \psi_{AT}| \tag{37}$$

At the onset of the HAC turn, the bank command is formed by merging feedforward and feedback terms. This command also incorporates the distance from the HAC center to maintain a constant turn radius.

$$\phi_{HAC} = \tan^{-1}\left(\frac{V_H^2 - \dot{R}^2}{gR_{HAC}}\right) + G_R^p \Delta R + G_R^d \Delta \dot{R} \tag{38}$$

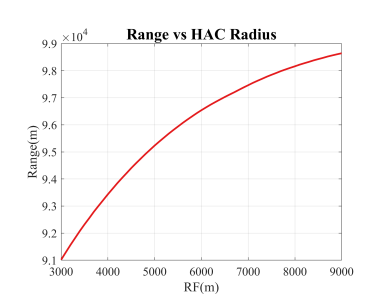
Upon completion of the HAC turn, control shifts to the pre-final phase once the heading error is maintained within  $5^{\circ}$ . In this phase, a PD law generates commands to reduce cross-range error relative to the runway centerline.

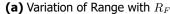
$$\phi_{PF} = -G_Y^p y - G_y^d \dot{y} \tag{39}$$

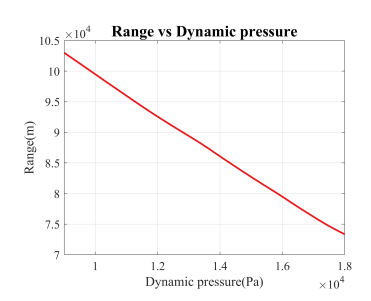
### 5. Cascade Predictor-Corrector Scheme

## 5.1. Sensitivity of Range to Adjustable Parameters

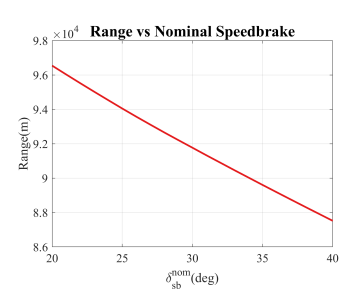
Prior to developing the Cascade Predictor–Corrector Scheme (CPCS), a sensitivity analysis was performed to quantify the influence of tunable parameters on the total flight range. As shown in Fig. 4, dynamic pressure provided the greatest range modulation authority ( $\sim$ 15 km). The next most effective was the speedbrake ( $\sim$ 5 km), followed by the HAC radius ( $\sim$ 4 km). This cascade of control authority defines the correction sequence. The reference dynamic-pressure profile is adjusted first for coarse range control. The HAC radius is then tuned to reduce residual errors. To maintain trajectory stability, the HAC radius is fixed once the HAC phase begins. After that point, only the speedbrake is used for fine error correction. Sensitivity results also guide the initial guess for the secant-method correction, enabling a warm start.







**(b)** Variation of Range with  $\bar{q}$ 



(c) Variation of Range with  $\delta_{sb}^{\text{nom}}$ 

Fig 4. Sensitivity of Range

### 5.2. Implementation Details

The CPCS architecture is shown in Fig. 5. At the start of TAEM, the algorithm decides between an overhead or direct trajectory based on the vehicle's state. After selecting the trajectory type, a two-stage correction begins. First, the dynamic pressure profile is adjusted to bring the range error within 100 m. Second, the HAC radius is tuned to reduce the remaining error to below 5 m. The final reference trajectory is then generated. Once the vehicle enters the HAC phase, the HAC radius is fixed. Any small errors are then corrected only by the speedbrake. The secant method is used throughout this process to solve for the correction variable (x), which can be dynamic pressure  $(\bar{q})$ , HAC radius  $(R_F)$ , or speedbrake deflection  $(\delta_{sb})$ . The solver is fast, typically converging in 2 to 6 iterations (under 0.5 seconds), well within the 4-second guidance cycle.

$$f(x) = s_{\text{total}} - s_{\text{pred}} \tag{40}$$

$$x^{k+1} = x^k - f(x^k) \frac{x^k - x^{k-1}}{f(x^k) - f(x^{k-1})}$$
(41)

Accurate prediction is critical for the CPCS. Large prediction errors can lead to poor corrections. To reduce this risk, the scheme compensates for aerodynamic forces in-flight, which are a major source of uncertainty. It uses onboard accelerometer data to calculate the lift-to-drag and drag ratios in real-time.

$$Z_{L/D}=rac{\hat{a}_L/\hat{a}_D}{ar{a}_L/ar{a}_D}$$
 (42)

$$Z_D = \hat{a}_D/\bar{a}_D \tag{43}$$

The drag ratio corrects for errors in air density and the drag coefficient, while the lift coefficient is adjusted using both the drag ratio and the lift-to-drag ratio. This ensures the predicted trajectory closely matches the vehicle's actual flight path.

$$C_D^{\mathsf{new}} = C_D \cdot Z_D \tag{44}$$

$$C_L^{\text{new}} = C_L \cdot Z_{L/D} \cdot Z_D \tag{45}$$

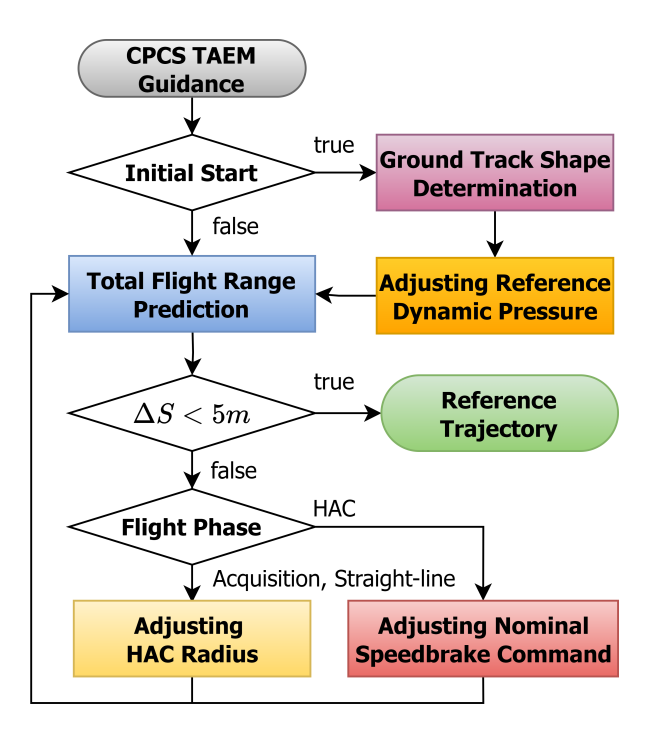


Fig 5. Cascade Predictor-Corrector Scheme

### 6. Numerical Simulations

#### 6.1. Nominal Simulation

The results of the nominal simulation, conducted using the boundary conditions defined in Table 1, are presented in Figs. 6 and 7. As shown in Fig. 6b, the vehicle successfully tracks the feasible reference dynamic pressure profile, with the speedbrake being actively deployed after the HAC turn to maintain precise tracking. Furthermore, the application of Eq. 45 and 44 yields highly accurate range predictions. As a result, all target conditions at the ALI point are satisfied, culminating in a final downrange error of 2.205 m and a crossrange error of 16.144 m.

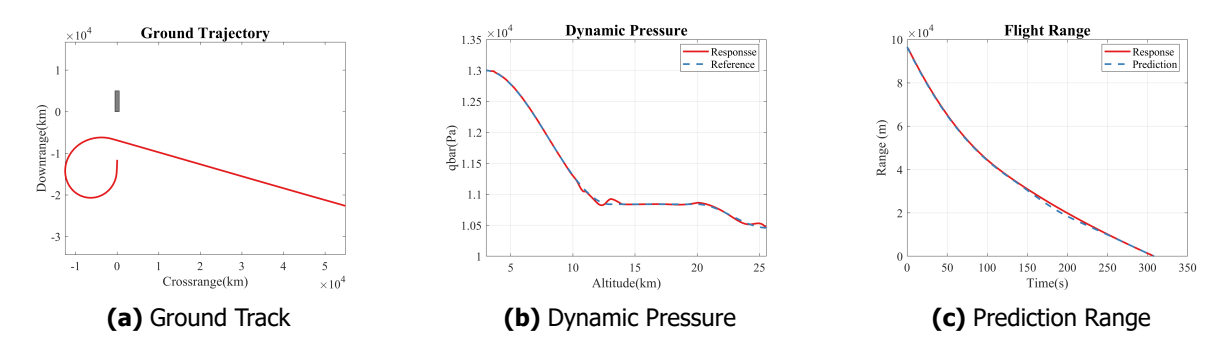


Fig 6. Results of Nominal Simulation

### 6.2. Monte Carlo Simulations

To evaluate the robustness of the proposed algorithm, 1,000 Monte Carlo simulations were conducted under the conditions summarized in Table 2. The simulations yielded a 99.2% success rate. Failures were attributed to cases where a feasible dynamic pressure profile for the designated runway could not be found, indicating the need for runway reassignment.

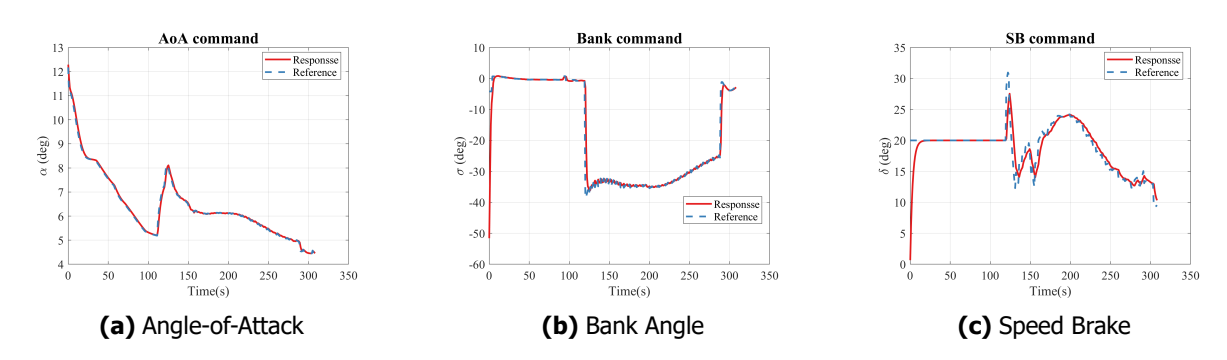


Fig 7. Control Inputs of Nominal Simulation

Variables	Distribution Type	3 $\sigma$ Error
$\lambda, \phi$	Gaussian	0.1 deg
V	Gaussian	30 m/s
$\gamma$	Gaussian	3 deg
$\psi$	Gaussian	15 deg
$C_L, C_D$	Gaussian	15 %
m	Gaussian	5 %
ρ	Gaussian	10 %
# of Simulations	1000	

Table 2. Monte Carlo Simulation Conditions

In all successful runs, the vehicle met the desired terminal conditions. Notably, Fig. 8 highlights the algorithm's effective energy management, showing that the final energy precisely matched the target value.

For comparison, the Space Shuttle guidance algorithm was tested under identical conditions (Fig. 9). In contrast to the CPCS, it frequently caused the vehicle to overshoot the ALI point and failed to converge on the target terminal energy.

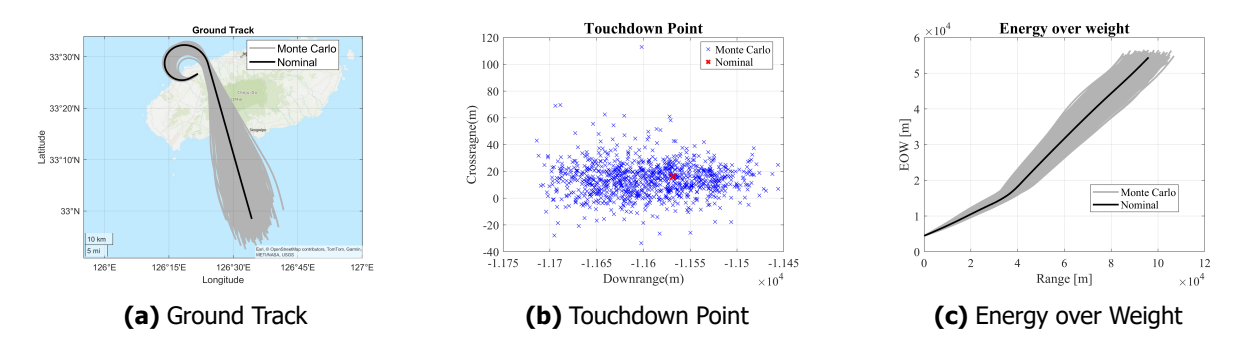


Fig 8. Monte Carlo simulations using CPCS

A quantitative comparison of the final position errors, provided in Table 3, confirms that the CPCS algorithm achieves consistently higher accuracy than the baseline Space Shuttle guidance.

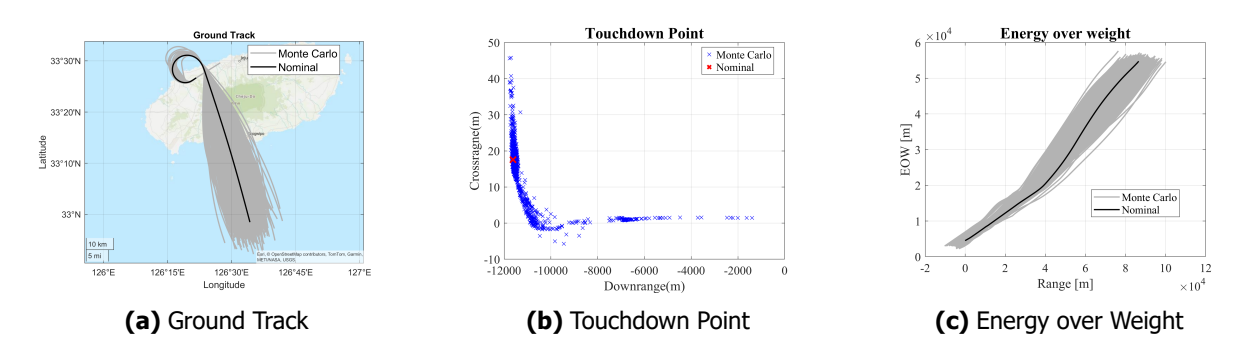


Fig 9. Monte Carlo simulations using Space Shuttle Guidance

Table 3. Position Error in ALI

Error	CPCS	Shuttle	
$- \Delta x $	50.5136 m	889.0017 m	
$- \Delta y $	15.5080 m	12.8810 m	

### 7. Conclusions

This paper introduced a Cascade Predictor-Corrector Scheme (CPCS) for the Terminal Area Energy Management (TAEM) phase of reusable space vehicles. The proposed guidance framework was designed to overcome the limitations of traditional offline methods and decoupled control strategies by systematically integrating ground-track generation, energy management, and in-flight trajectory correction.

An optimization-based analysis identified the Space Shuttle ground track as a near-optimal solution, which served as the foundation for the lateral guidance law. A key contribution of this work is the development of a cascade correction logic, motivated by a sensitivity analysis that quantified the range control authority of dynamic pressure, HAC radius, and speedbrake deflection. This hierarchical approach enables efficient coarse-to-fine adjustments, ensuring the vehicle meets terminal conditions with high precision. Furthermore, the integration of an aerodynamic model correction using real-time lift-to-drag and drag ratio estimates significantly improved the accuracy of range predictions, enhancing the robustness of the algorithm.

Numerical simulations demonstrated the effectiveness of the CPCS. In the nominal case, the algorithm successfully tracked the reference profiles and achieved terminal errors of approximately 2.2 m in down-range and 16.1 m in cross-range. More importantly, extensive Monte Carlo simulations confirmed the algorithm's robustness, yielding a 99.2% success rate under significant initial condition and model uncertainties. A direct comparison revealed the superior performance of the CPCS over the legacy Space Shuttle guidance, particularly in terminal accuracy and energy management.

In conclusion, the proposed CPCS has demonstrated its capability to precisely guide a reusable space vehicle to the ALI by effectively managing its energy state. The applicability of this framework extends beyond RSV to a broader class of gliding vehicles that require high-precision terminal guidance. Future work will be directed towards enhancing the convergence speed and stability of the Predictor-Corrector algorithm. Furthermore, the research will be expanded to address more comprehensive mission scenarios, including dynamic events such as in-flight runway reallocation, to further validate the robustness and operational feasibility of the proposed guidance law.

## **Acknowledgment**

This work has been supported by the Korea Aerospace Research Institute (KARI)'s research project entitled "Development of Control Performance Analysis Program for Spaceplanes."

### References

- [1] Grantz, A.: X-37b Orbital Test Vehicle and Derivatives. In: AIAA SPACE 2011 Conference & Exposition, p. 7315. American Institute of Aeronautics and Astronautics, Long Beach, CA (2011). https://doi.org/10.2514/6.2011-7315
- [2] Bergman, C., Gavert, D., de la Torre, R., Owen, D., Bateman, D.: Entry Through Landing Guidance. Technical report (December 2007)
- [3] Moore, T.E.: Space shuttle entry terminal area energy management. Technical Report S-661, NASA Johnson Space Center, Houston, TX (November 1991)
- [4] Grubler, A.C.A.C.: New methodologies for onboard generation of Terminal Area Energy Management trajectories for autonomous reusable launch vehicles. Thesis, Massachusetts Institute of Technology, Cambridge, MA (2001)
- [5] Horneman, K., Kluever, C.: Terminal Area Energy Management Trajectory Planning for an Unpowered Reusable Launch Vehicle. In: AIAA Atmospheric Flight Mechanics Conference and Exhibit, p. 5183. American Institute of Aeronautics and Astronautics, Providence, RI (2004). https://doi.org/10.2514/6.2004-5183
- [6] Hull, J., Gandhi, N., Schierman, J.: In-Flight TAEM/Final Approach Trajectory Generation for Reusable Launch Vehicles. In: Infotech@Aerospace, p. 7114. American Institute of Aeronautics and Astronautics, Arlington, VA (2005). https://doi.org/10.2514/6.2005-7114
- [7] Kluever, C., Horneman, K., Schierman, J.: Rapid Terminal-Trajectory Planner for an Unpowered Reusable Launch Vehicle. In: AIAA Guidance, Navigation, and Control Conference, p. 5766. American Institute of Aeronautics and Astronautics, Chicago, IL (2009). https://doi.org/10.2514/6.2009-5766
- [8] Lan, X.-J., Liu, L., Wang, Y.-J.: Online trajectory planning and guidance for reusable launch vehicles in the terminal area. Acta Astronautica **118**, 237–245 (2016) https://doi.org/10.1016/j.actaastro.2015.10.019
- [9] Mu, L., Yu, X., Zhang, Y., Li, P., Wang, X.: Trajectory Planning for Terminal Area Energy Management Phase of Reusable Launch Vehicles. IFAC-PapersOnLine 49(17), 462–467 (2016) https://doi.org/10.1016/j.ifacol.2016.09.079
- [10] Lan, X., Xu, W., Wang, Y.: 3D Profile Reconstruction and Guidance for the Terminal Area Energy Management Phase of an Unpowered RLV with Aerosurface Failure. Journal of Aerospace Engineering **33**(3), 04020003 (2020) https://doi.org/10.1061/(ASCE)AS.1943-5525.0001112
- [11] Kluever, C.A.: Simple Analytical Terminal Area Guidance for an Unpowered Reusable Launch Vehicle. Journal of Guidance, Control, and Dynamics **45**(4), 740–747 (2022) https://doi.org/10.2514/1.G006338
- [12] Yang, T., Qiu, J., Liu, L., Wang, Y.: Online trajectory design for Terminal Area Energy Management of Reusable Launch Vehicle. In: 2016 IEEE Chinese Guidance, Navigation and Control Conference (CGNCC), Nanjing, China, pp. 2032–2036 (2016). https://doi.org/10.1109/CGNCC.2016.7829103
- [13] Mayanna, A., Grimm, W., Well, K.: Adaptive Guidance for Terminal Area Energy Management (TAEM) of Reentry Vehicles. In: AIAA Guidance, Navigation, and Control Conference and Exhibit, p. 6037. American Institute of Aeronautics and Astronautics, Keystone, CO (2006). https://doi.org/10.2514/6.2006-6037
- [14] Jiang, W., Yang, Z.: Guidance Law Design for Terminal Area Energy Management of Reusable Launch Vehicle by Energy-to-Range Ratio. Mathematical Problems in Engineering **2014**(1), 929731 (2014) https://doi.org/10.1155/2014/929731